









# On the origin of the environmental step: A BayeSN view of the ZTF SN Ia DR2

Madeleine Ginolin<sup>1\*</sup>, Matthew Grayling<sup>1</sup>, Kaisey S. Mandel<sup>1,2</sup>, Maximilian Autenrieth<sup>1,2</sup>,  
Benjamin M. Boyd<sup>1</sup>, Aaron Do<sup>1</sup>, Lisa Kelsey<sup>1</sup>, Matthew O’Callaghan<sup>1</sup>

<sup>1</sup>*Institute of Astronomy and Kavli Institute for Cosmology, University of Cambridge, Madingley Road, Cambridge CB3 0HA, UK*

<sup>2</sup>*Statistical Laboratory, DPMMS, University of Cambridge, Wilberforce Road, Cambridge, CB3 0WB, UK*

Last updated —; in original form —

## ABSTRACT

Astrophysical variabilities of Type Ia supernovae (SNe Ia) are now one of the leading sources of systematic uncertainties on the measurement of the dark energy equation-of-state parameter  $w$ . Population studies of SNe Ia give precious insights into these variabilities. We analyse a volume-limited subsample of the ZTF SN Ia DR2 with BayeSN, a hierarchical Bayesian model for SN Ia SEDs. We investigate the distributions of SN Ia light curve parameters and their link with SN environment. Using a new training of BayeSN, we find a smaller scatter of Hubble residuals compared to SALT. We then investigate the magnitude step, which accounts for the correlation between SN Ia standardised absolute magnitude and host environments. We find a posteriori steps of  $0.103 \pm 0.010$  mag (a  $10.1\sigma$  difference from 0) when using global stellar mass as an environmental proxy, and  $0.086 \pm 0.010$  mag ( $8.3\sigma$ ) when using local colour. This confirms that the large steps seen in ZTF were not due to the SALT fits or the standardisation process. We then investigate the origin of the step, using a BayeSN model which accounts for both an intrinsic magnitude step and differing dust properties with the SN environment. We find a  $0.103 \pm 0.018$  mag ( $5.6\sigma$ ) step in global mass and a  $0.085 \pm 0.019$  mag ( $4.5\sigma$ ) step in local colour. The means of the  $R_V$  distribution are similar between different host environments, with  $\Delta E(R_V) \leq 0.2$  across all environment proxies. This is a strong signal of the existence of an intrinsic step.

**Key words:** supernovae: general - cosmology: distance scale - dust, extinction - methods: statistical

## 1 INTRODUCTION

Type Ia supernovae (SNe Ia) are one of the most used tools to measure distances in the Universe, as their peak absolute magnitudes are, at first order, a constant, making them *standard* candles. They have been instrumental in the discovery of the acceleration of the expansion of the Universe (Riess et al. 1998; Perlmutter et al. 1999). They are still key in measurements of cosmological parameters, such as the Hubble constant  $H_0$  (Freedman 2021; Riess et al. 2022) and the dark energy equation-of-state parameter  $w$  (DES Collaboration et al. 2024; Rubin et al. 2023). As such, they are at the heart of two puzzles of today’s cosmology: the Hubble tension, a persistent mismatch of  $H_0$  between local measurements and constraints from the Cosmic Microwave Background (see e.g. Di Valentino et al. 2025), and the recent tentative detection of an evolution of  $w$  with cosmic time (Adame et al. 2025; DESI Collaboration et al. 2025).

In reality, SNe Ia are *standardisable* candles: their peak absolute magnitudes exhibit a natural scatter of  $\sim 0.4$  mag. In order to reduce this scatter, to increase the precision of distance measurements derived from SNe Ia, an empirical standardisation was progressively developed. This process exploits correlation of the peak absolute magnitude with light curve properties e.g. its width (Phillips 1993) and its colour (Tripp 1998), reducing this scatter to  $\sim 0.15$  mag. An

additional standardisation parameter was added in the early 2010s, which accounts for correlations between the host environment of the SN and its (standardised) absolute magnitude (Kelly et al. 2010; Sullivan et al. 2010; Lampeitl et al. 2010; Childress et al. 2013). Originally dubbed the mass step, as it was based on the stellar mass of the host galaxy of the SN, studies of this dependency have grown more numerous in recent years. For example, different tracers to measure this step have been investigated, and in particular tracers local to the SN, thought to measure more accurately its environment (Rigault et al. 2020; Briday et al. 2022; Kelsey et al. 2021). While it is now usually included in cosmological analyses (Betoule et al. 2014; Brout et al. 2022; DES Collaboration et al. 2024), the incorrect or partial correction of its effect might bias cosmological parameter inference (Rigault et al. 2015). Moreover, the origin of this step is still debated. While some argue that it is linked to an intrinsic difference of SN Ia, such as differences in the progenitor system, e.g. age, metallicity, explosion mechanisms... (Rigault et al. 2020; Briday et al. 2022; Kim et al. 2018; Sarin et al. 2026; Magee 2026), another hypothesis has arose in recent years, attributing this step to different dust properties in different host environments (Brout & Scolnic 2021; Popovic et al. 2023). In reality, it is likely that the environmental step is a mixture of both effects (Wiseman et al. 2022; Thorp et al. 2021; Thorp & Mandel 2022; Kelsey et al. 2023; Popovic et al. 2024; Grayling et al. 2024; Hayes et al. 2025).

SN Ia properties also correlate with the astrophysical environment

\* Contact e-mail: [madeleine.ginolin@ast.cam.ac.uk](mailto:madeleine.ginolin@ast.cam.ac.uk)

in which they exploded. The correlation between SN stretch, an intrinsic light curve property, and environment, where older and redder galaxies host faster evolving SNe on average (Filippenko 1989; Hamuy et al. 1996; Sullivan et al. 2010; Rigault et al. 2020), has been known since the 90s. In recent years, in-depth studies of this correlation were published, along with the development of analytical models (Nicolas et al. 2021; Ginolin et al. 2025b). Most of these are based on a two-population SN Ia model (Mannucci et al. 2006; Sullivan et al. 2006; Smith et al. 2012; Childress et al. 2014; Rigault et al. 2013), similar to the intrinsic difference postulated as the origin of the step. On the other hand, SN light curve colour is thought to be a mixture of intrinsic SN colour variations due to the explosion physics of the SN and dust reddening (Jha et al. 2007; Mandel et al. 2017; Uddin et al. 2020; Duarte et al. 2023), which will necessarily change with environment (Brout & Scolnic 2021; Popovic et al. 2023, 2025b). This is also translated through the expected variation of the colour standardisation parameter  $\beta$  with host galaxies parameters, e.g. host mass (Sullivan et al. 2010; Amanullah et al. 2010; Mandel et al. 2017; González-Gaitán et al. 2021; Brout & Scolnic 2021; Rubin et al. 2023, 2026).

Most of the analyses cited in the previous paragraphs have been based on SALT light curve fits (Guy et al. 2005, 2007; Betoule et al. 2014; Kenworthy et al. 2021). While SALT is widely used in cosmological analyses, its model of SN Ia SED is mostly empirical. In particular, SALT colour attempts to encapsulate both intrinsic and extrinsic colour within a single apparent colour parameter  $c$ , without leveraging our understanding of dust reddening. Correctly modelling for dust is crucial for a precise determination of cosmological parameters, as it is now one of the dominating systematics in the  $w$  error budget (Vincenzi et al. 2024). BayeSN (Mandel et al. 2022; Thorp et al. 2021) solves this issue by explicitly including the impact of dust on the intrinsic SN Ia SED. It can thus provide precious insights on the distribution of SNe properties and the associated dust properties, as well as on the origin of the environmental step, as was done in Thorp & Mandel (2022); Grayling et al. (2024).

We here analyse the ZTF sample with BayeSN. We use the same selection cuts as in Ginolin et al. (2025a,b), to be able to cross-check results with this SALT-based analysis. In particular, we use a volume-limited subsample of the DR2, which is designed to make non-random selection effects negligible.

We provide a brief description of BayeSN in Sec. 2, as well as the particular model used in this analysis, described in Grayling et al. (in prep), hereafter G26. We present in Sec. 3 the data used. In Sec. 4, we show BayeSN fits of the ZTF light curves. We investigate the two light curve properties,  $A_V$  and  $\theta_1$ , as well as the Hubble residuals, and compare the results with the SALT-based analysis of Ginolin et al. (2025a,b). In Sec. 5, we focus on the magnitude step, using a BayeSN model which includes dust variations across environments. We discuss these results and analysis variations in Sec. 6. We conclude in Sec. 7.

## 2 BAYESN

BayeSN is a hierarchical Bayesian model of SN Ia at the SED level, which describes a population of SNe, and samples a posterior of both population-level and individual-supernova parameters. The BayeSN framework is described in Mandel et al. (2022) (building upon previous hierarchical SN Ia light curve models of Mandel et al. 2009, 2011), and a first training was released in Thorp et al. (2021), hereafter T21. The current BayeSN code, based on the `numpyro` implementation described in Grayling et al. (2024), is publicly available

and documented<sup>1</sup>. We provide in Sec. 2.1 a brief general description of the BayeSN model, and introduce the G26 training, used in this analysis in Sec. 2.2.

### 2.1 Description of the model

In the BayeSN model, the SED of a given SN, indexed as  $s$ , is written as:

$$-2.5 \log \left( \frac{S^s(t, \lambda)}{S_0(t, \lambda)} \right) = M_0 + \delta M^s + W_0(t, \lambda) + \theta_1^s W_1(t, \lambda) + A_V^s \xi(\lambda; R_V^{(s)}) + \epsilon^s(t, \lambda), \quad (1)$$

where  $t$  is the rest-frame  $B$ -band phase, and  $\lambda$  is the rest-frame wavelength. Here, and throughout the paper,  $\log$  denotes the decimal logarithm. The base template  $S_0(t, \lambda)$  is the Hsiao et al. (2007) SED template combined with a normalisation constant  $M_0$ , fixed at  $-19.5$  mag. The rest of the components of the model are described below:

- $\delta M^s$  is a per-SN achromatic offset, drawn from a normal distribution, such as  $\delta M^s \sim N(0, \sigma_0^2)$ . This term captures the unexplained scatter of peak absolute magnitude, parametrised by an intrinsic scatter  $\sigma_0$ .
- $W_0(t, \lambda)$  and  $W_1(t, \lambda)$  are respectively the 0<sup>th</sup> and 1<sup>st</sup> order functional principal component (FPC) of the SED, implemented as cubic spline surfaces.
- $\theta_1^s$  is a per-SN coefficient that quantifies the impact of  $W_1$  on the final SED. It is correlated to the width of the light curve, and as such the product of  $\theta_1^s$  and  $W_1$  reproduces the 'broader-brighter' relation (Phillips 1993), where slower evolving SNe, which have broader light curves at peak, are on average brighter than fast-evolving SNe. We use a Gaussian prior on  $\theta_1$ , so that  $\theta_1 \sim N(0, 1)$ .
- $\xi(\lambda; R_V^{(s)})$  is the dust extinction law, here from Fitzpatrick (1999), parametrised by  $R_V^{(s)}$ .  $R_V$  can either be treated as a population parameter, or be fitted individually for each SN. We use a fixed  $R_V$  for Section 4, and we investigate the use of a per-SN  $R_V^s$  in Sec. 5.
- $A_V^s$  is the per-SN dust extinction in V-band. It is assigned an exponential prior, parametrised by a population parameter  $\tau_A$ , so that

$$P(A_V^s | \tau_A) = H(A_V^s) \times \tau_A^{-1} \exp(-A_V^s / \tau_A) = \begin{cases} \tau_A^{-1} \exp(-A_V^s / \tau_A) & \text{if } A_V^s \geq 0, \\ 0 & \text{if } A_V^s < 0. \end{cases}$$

where  $H$  is the Heaviside function.

- $\epsilon^s(t, \lambda)$  is a per-SN term that captures the intrinsic colour variations unaccounted for by the dust term  $A_V^s \xi(\lambda; R_V^{(s)})$ . It is represented by a cubic spline over two dimensions, defined by a matrix of knots  $\mathbf{E}^s$ , drawn from a multivariate Gaussian  $e^s \sim N(0, \Sigma_\epsilon)$ . Here  $e^s$  is the vectorisation of  $\mathbf{E}^s$ , and  $\Sigma_\epsilon$  is a covariance matrix, inferred as a hyperparameter during the training stage of the model.

The resulting SED is then corrected for Milky-Way extinction, scaled to the distance modulus  $\mu^s$ , and can then be integrated through bandpasses to produce photometric points, which are then compared to measured light curve data.  $\mu^s$  is fitted using a prior which combines redshift information and an assumed cosmology. This choice allows for magnitude information to be used as an additional constraint on dust properties when training, which is especially useful in cases where the wavelength coverage of the data is relatively narrow,

<sup>1</sup> <https://bayesn.readthedocs.io/>

such as in the ZTF dataset (see Sec. 3). The distance modulus is thus conditioned as  $P(\mu^s | z^s) = N(\mu_{\text{cosmo}}(z^s), (\sigma_{\mu}^s)^2)$ , where  $\mu_{\text{cosmo}}$  is computed assuming a flat  $\Lambda$ CDM Universe with  $\Omega_m = 0.28$  and  $H_0 = 73.24 \text{ km s}^{-1} \text{ Mpc}^{-1}$ , and  $(\sigma_{\mu}^s)^2 \approx (\frac{5}{z \ln 10})^2 [(\sigma_z^s)^2 + \sigma_{\text{pec}}^2/c^2]$ , where  $\sigma_z^s$  is the redshift uncertainty and  $\sigma_{\text{pec}} = 150 \text{ km s}^{-1}$  is the peculiar velocity dispersion (Carrick et al. 2015). While the assumption of a cosmology would need to be considered when using BayeSN on high redshift and magnitude-limited samples, this is not a concern here. Indeed, we use a low-redshift sample, for which the distance modulus is only marginally sensitive to values of cosmological parameters, in its volume-limited version (see Sec. 3.2), essentially removing any selection bias.

BayeSN works in two modes: fitting and training. When fitting data with a pre-trained model, we only infer individual SN properties, denoted by the superscript  $s$  ( $A_V^s$ ,  $\theta_1^s$ ,  $\delta M^s$  and  $\epsilon^s$ ). As we do not need to infer population-level dust properties ( $R_V$  and  $\tau_A$ ), distances are kept as a free parameter and no cosmology-dependent prior is used. We use the fitting mode in Sec. 4. In Sec. 5, we partially train the model to jointly infer per-SN properties and population-level dust parameters. We however keep  $W_0$ ,  $W_1$ ,  $\sigma_0$  and  $\Sigma_{\epsilon}$  fixed to their model value. We note that in that section, we infer an individual  $R_V^s$  for each SN. We discuss the full training of BayeSN with ZTF in Sec. 6.5.

In each of the runs of this analysis, we infer the posteriors of the parameters using MCMC sampling. We use four chains initialised at different locations of the parameter space. Each chain is run for 500 steps, including 250 warm-up steps. For every analysis, we evaluate the convergence of the chains, both by visually inspecting them (especially when inferring model hyperparameters), and by computing the potential scale reduction factor  $\hat{R}$  for each parameters.

## 2.2 BayeSN-Dovekie model

In our fiducial analysis, we use the soon-to-be released G26 BayeSN model (not to be confused with the recent extended-phase optical-NIR BayeSN model used for lensed SNe Ia from Grayling et al. 2026). This model was obtained using a framework that simultaneously trains a SED model in a BayeSN-like fashion, and cross-calibrates bandpasses across different surveys in a Dovekie-like fashion (Popovic et al. 2025a). Cross-calibration puts bandpasses in a common photometric system, and is necessary when using multiple surveys, and thus multiple observing systems. The cross-calibration (filter offsets and shifts) is obtained using information from the SNe Ia themselves, combined with priors coming from previous Dovekie runs.

G26 also used different data than the fiducial T21 training. T21 used 157 SNe from Foundation Foley et al. (2018), while G26 uses three low-redshift surveys (Foundation, CSP from Krisciunas et al. 2017, CfA3-4 from Hicken et al. 2009a,b, 2012), along with four higher-redshift surveys (PS1 from Jones et al. 2018, SDSS from Holtzman et al. 2008, SNLS from Astier et al. 2006, DES from Abbott et al. 2019), totalling 1024 SNe. We evaluate the impact on our results of the BayeSN training used in Sec. 6.1.

## 3 DATA

In this paper, we use the second SN Ia release of the Zwicky Transient Facility (ZTF, Bellm et al. 2019; Graham et al. 2019; Masci et al. 2019; Dekany et al. 2020). ZTF is a low-redshift transient photometric survey, observing the northern sky. It uses three bands ( $g$ ,  $r$  and  $i$ ), and can detect SNe Ia up to  $z \sim 0.1$ . It additionally comprises

a dedicated low-resolution integral field spectrograph, the SEDmachine (Blagorodnova et al. 2018; Rigault et al. 2019), optimised for the spectroscopic typing of transients.

### 3.1 ZTF SN Ia DR2

The ZTF SN Ia DR2, described in details in Rigault et al. (2025), is composed of all spectroscopically typed SNe Ia observed by ZTF between March 2018 and December 2020. The spectroscopic typing was done mostly with spectra coming from the BTS survey (Perley et al. 2020). The data made publicly available includes the light curves of the SNe, as well as their SALT2.4 fits (Guy et al. 2007, 2010; Betoule et al. 2014; Taylor et al. 2021).

Each SN also has an associated redshift, coming either from a spectrum of its host galaxy (61%), from host galaxy features in the SN spectra (9%) or from SN spectral features themselves (30%).

Alongside with SN data, host galaxies and environmental properties were also released. The host matching was done using the  $d_{\text{DLR}}$  technique (Sullivan et al. 2006; Gupta et al. 2016), where  $d_{\text{DLR}}$  is the normalised distance of the SN to its host. The host galaxies were fitted with HostPhot (Müller-Bravo & Galbany 2022) on Pan-STARRS (Chambers et al. 2016) photometry. The derived properties are global stellar mass and  $(g - z)$  colour, and local stellar mass and  $(g - z)$  colour, computed with an aperture of a 2 kpc radius around the SN.

The ZTF SN Ia DR2 is not yet cosmology ready, due to known non-linearities and a photometric accuracy not yet sufficient for cosmological analysis (Lacroix et al. 2025). We discuss the possible uses of the next release of ZTF, which fixes these issues, in Sec. 6.5.

### 3.2 Volume-limited sample

We here use a volume-limited sample of the ZTF SN Ia DR2, designed to minimise any observational biases, such as the Malmquist bias. We thus only use SNe up to  $z = 0.06$  (Amenouche et al. 2025). We additionally use the same quality cuts as those described in Ginolin et al. (2025a,b), so that our samples are identical. These cuts are the following:

- Light curve sampling: we keep SNe with seven detections (at the  $5\sigma$  level) in the  $[-10, 40]$  days phase range, in at least two bands and with at least two detections before peak and two detections after peak.
- SALT fit: we keep SNe with a light curve fit probability greater than  $10^{-7}$ . We also impose that the SALT stretch  $x_1$  is in  $[-3, 3]$ , measured with a precision  $\sigma_{x_1} < 1$ , that the SALT colour  $c$  is in  $[-0.2, 0.8]$  measured with a precision  $\sigma_c < 0.1$ . We finally impose that the error on the fitted time of peak luminosity  $T_0$  is lower than one day.
- SN Ia subtype: we remove peculiar SNe Ia, such as 91bg or Ia-CSM, but keep the 91t.

Objects without host measurements (either local or global) are also removed from this sample.

The final sample comprises 932 objects. The list of every SN passing the cuts is available on GitHub<sup>2</sup>.

We note that some objects were discarded from the sample on the basis of bad or extrapolated SALT fits, which might not be the case with BayeSN. We make this choice to allow for a meaningful comparison of the two fitting methods.

<sup>2</sup> [http://github.com/mginolin/standax/blob/main/notebooks/Ginolin25ab\\_masterlist.csv](http://github.com/mginolin/standax/blob/main/notebooks/Ginolin25ab_masterlist.csv)

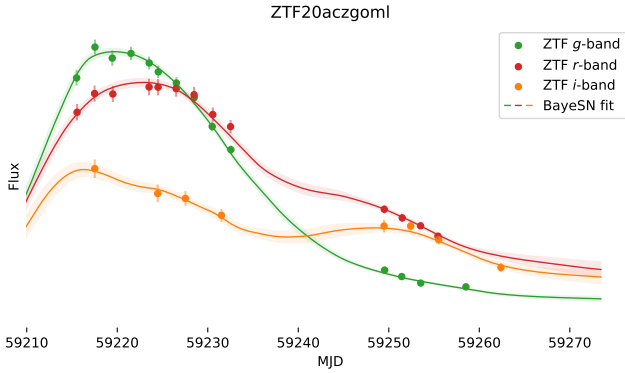


**Figure 1.** BayeSN fit of a randomly selected ZTF SN. The solid lines are the posterior mean of the model, while the shaded bands show the standard deviation of the chains.

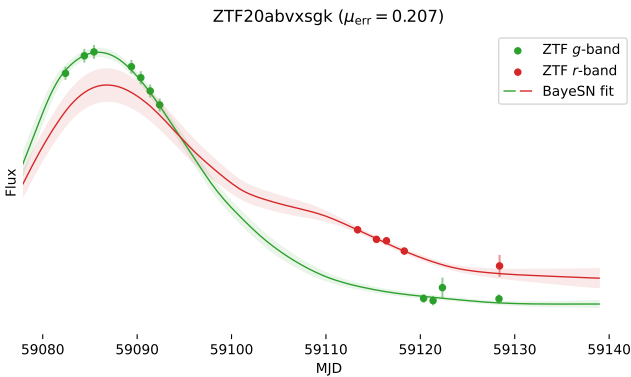


**Figure 2.** Example of a 'bad' BayeSN fit, defined as having an error on distance moduli larger than  $\mu_{\text{err}} > 0.2$ .

### 3.3 Preprocessing of the light curves

In order to use the publicly available light curves, some preprocessing is needed. The first step is to output the light curves at a zero point of  $ZP = 27.5$ , to match the value expected by BayeSN. We then apply the quality cuts used in Rigault et al. (2025), as implemented in the `lightcurve.get_lcd_data()` function from the `ztfcosmo` library. To speed up the fitting of the light curves and to limit memory usage, we use the same averaging recipe as the one used for the DR2 SALT fits, which performs averaging in 12h rolling bins. Finally, we apply the per-band error floors from Amenouche et al. (2025). We also compute CMB-frame redshifts, following Carr et al. (2022).

## 4 LIGHT CURVE FITS

We start by fitting the DR2 volume-limited sample using the G26 BayeSN retraining presented in Sec. 2.2. The fitting of the 932 light curves takes around 30 mins when using four GPUs and a standard MCMC sampling. A variational inference (VI) implementation of the fitting is also available (Uzsoy et al. 2024), but as our sample is of a reasonable size the speed-up enabled by VI is not necessary here. We present an example of a light curve fit in Fig. 1. As expected, as we are dealing with an already selected sample, all of the fits are reasonably good, e.g. the MCMC chains are converged and well

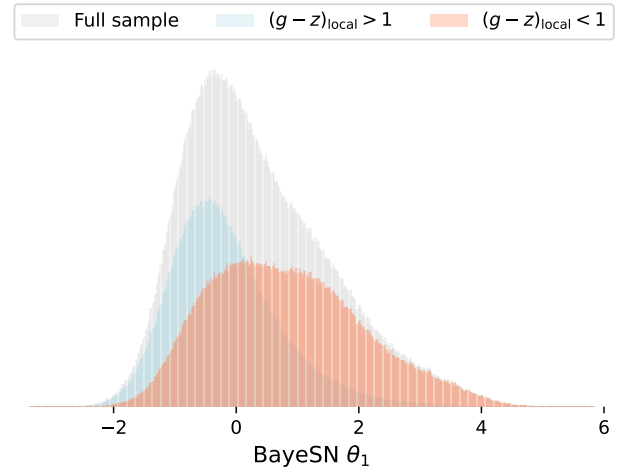


**Figure 3.** Histogram of BayeSN  $\theta_1$ . The full sample is plotted in grey, while the blue and red distribution correspond to SNe in locally blue and red environment, as defined in Sec. 4.2.1. To showcase both the population spread and the posterior uncertainty on  $\theta_1$  for individual SNe, we use values from the full MCMC chains, minus warm-up, which results in 1,000 steps per SN.

mixed. As an extra precaution, we manually check the few problem cases with large errors on the distance modulus ( $\mu_{\text{err}} > 0.2$ ). These seem to come from the lesser sampled light curves, or ones with only two bands ( $g$  and  $r$ ), as illustrated in Fig. 2. We thus conclude that we do not have to discard any extra SNe based on their BayeSN fit.

### 4.1 Distribution of the parameters

We now look at the distributions of the light curve parameters  $\theta_1$  and  $A_V$ . In this section, to compare with the ZTF sample investigated in Ginolin et al. (2025a,b), we apply the same outlier rejection, which discards 7 objects based on a cut on Chauvenet's criterion on the standardised Hubble residuals.

#### 4.1.1 Light curve width $\theta_1$

As seen in Fig. 3, the distribution of  $\theta_1$  for the full sample is non-Gaussian, with a second bump arising around  $\theta_1 \sim 1$ . This is similar to the behaviour of SALT stretch, and expected seeing their strong correlation (see Sec. 4.3). As  $\theta_1$  is constrained by a Gaussian prior  $\mathcal{N}(0, 1)$ , we manually look at the very large  $\theta_1$  cases, in which it is far away from its prior. Those fits are reasonable, and correspond to very low SALT  $x_1$  SNe. The existence of a large out-of-prior population might be due to a lower average stretch, corresponding to a higher average  $\theta_1$ , in the ZTF sample compared to the BayeSN training sample.

#### 4.1.2 Dust extinction $A_V$

We plot on the top of Fig. 4 the distribution of  $A_V$  for the full sample. Most of the SNe have an  $A_V$  below 0.5, but the tails extends to value up to  $A_V \sim 1$ . As we are using a volume-limited sample, it is expected that we observe redder SNe on average, i.e. larger  $A_V$  values, that might be missing from magnitude-limited samples.

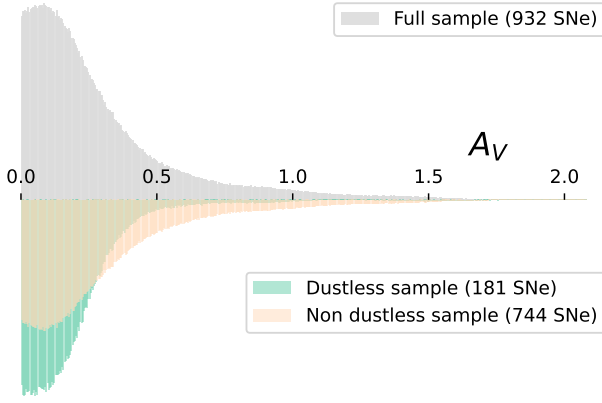


**Figure 4.** *Top:* Histogram of BayeSN  $A_V$ . *Bottom:*  $A_V$  distributions for dustless and dusty subsamples, as defined in Sec. 4.2.2.

## 4.2 Dependence on environment

### 4.2.1 $\theta_1$

We plot in Fig. 3 the  $\theta_1$  distributions for locally blue and red environments, defined as  $(g - z)_{\text{local}} \leq 1$ . As expected, due to its link with the decline rate of the light curves,  $\theta_1$  is strongly correlated with the host environment of the SN. In particular, SNe in locally red environments extend to larger values of  $\theta_1$ .

### 4.2.2 $A_V$

We then reproduce Fig. 1 from Ginolin et al. (2025a), where the colour distribution is split between a “dustless” sample and a non-dustless sample. The dustless sample is defined by objects in locally low stellar mass regions ( $\log(M_*/M_\odot) < 8.9$ ) and in the outskirts of their host galaxy ( $d_{\text{DLR}} > 1.2$ ).<sup>3</sup> The distance to the host galaxy is defined with the dimensionless Directional Light Ratio  $d_{\text{DLR}}$  (Sullivan et al. 2006; Gupta et al. 2016), a normalised measure of distance of the SN to the centre of the host, robust to different galaxy sizes and inclination effect. The non-dustless sample comprises of every SNe which are not in the dustless sample. Due to projection effects, SNe in this sample might also be unaffected by dust, which is why we do not name it the dusty sample. We see in the bottom of Fig. 4 that all high  $A_V$  objects live in the non-dustless sample, as expected. However, as noted in Ginolin et al. (2025a), the dustless sample seems to still be affected by dust, as some of the  $A_V$  values depart from 0. This is true if  $A_V$  only encapsulates dust effect, and none of the intrinsic colour scatter present in the ZTF sample, as investigated in Sec. 4.3. The direct determination of  $A_V$  made possible by BayeSN could lead to a more straightforward cut to isolate SNe relatively unaffected by dust, leading to a sample easier to standardise, with reduced systematic errors.

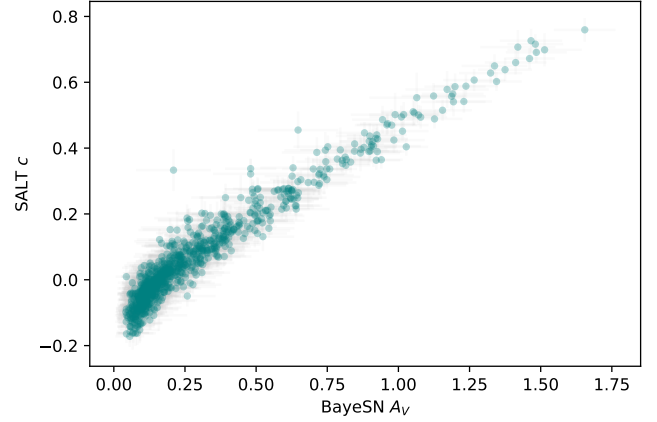


**Figure 5.** SALT colour  $c$  against BayeSN extinction  $A_V$ .

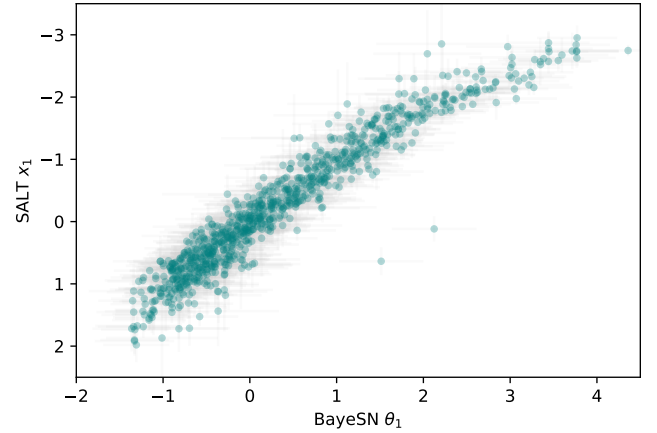


**Figure 6.** SALT stretch  $x_1$  against BayeSN  $\theta_1$ . Note that the  $x_1$  axis is reversed.

## 4.3 SALT comparison

We plot in Figs. 5-6 the comparison between the BayeSN parameters ( $\theta_1$  and  $A_V$ ) and their SALT equivalents ( $x_1$  and  $c$ ). While these parameters are not a one-to-one match, this comparison is still interesting, as most of the literature on SN light curve properties, standardisation and their link with environment is based on SALT fits.

Looking at Fig. 5, BayeSN  $A_V$  and  $c$  look strongly correlated. However, even at a null  $A_V$ , we see a scatter in  $c$ , which might point to a non-null intrinsic colour scatter. Fitting a Gaussian on the SALT  $c$  distribution for SNe with  $A_V < 0.1$ , we find a standard deviation of  $0.027 \pm 0.004$  and a mean of  $-0.083 \pm 0.004$ . This is in accordance with the Gaussian intrinsic colour distribution fitted in Ginolin et al. (2025a), of width  $0.030 \pm 0.005$  and mean  $-0.085 \pm 0.004$ .

There is also a strong inverse correlation between  $\theta_1$  and  $x_1$ , which however seems non-linear, as visible in Fig. 6. The non-linearity of

<sup>3</sup> This value differs from the one used in Ginolin et al. (2025a), as a small change in  $d_{\text{DLR}}$  values was not propagated through the dataset used in this analysis. We thus adapt the value of the cut to match the statistics of the dustless sample in Ginolin et al. (2025a).

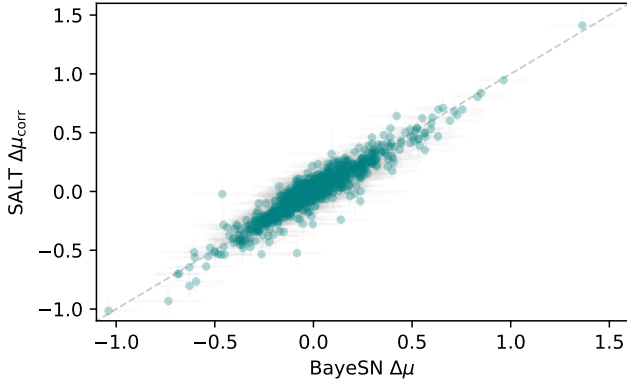


**Figure 7.** Standardised SALT Hubble residuals against BayeSN Hubble residuals, as described in Sec. 4.4.

**Table 1.** Hubble residuals scatter for BayeSN output  $\mu_{\text{res}}$  and standardised SALT outputs. We use both the regular standard deviation  $\sigma_{\text{STD}}$  and the normalised median absolute deviation  $\sigma_{\text{nMAD}}$ . The host- $z$  subsample (729/929 SNe) is defined as objects with a redshift from host galaxy features, either from galaxy lines in the SN spectrum or from a spectrum of the host galaxy itself.

Scatter	Full sample		Host- $z$ sample	
	BayeSN	SALT	BayeSN	SALT
$\sigma_{\text{STD}}$	0.225	0.230	0.204	0.213
$\sigma_{\text{nMAD}}$	0.177	0.181	0.165	0.169

this relation is partly due to the fact that  $\theta_1$  is a linear effect on log-flux, while  $x_1$  is a linear effect on flux. It also might be a consequence of the non-linearity of the SALT stretch-residuals relation found in [Ginolin et al. \(2025b\)](#), where the Hubble residuals for low-stretch (i.e. high  $\theta_1$ ) SNe have a stronger correlation with stretch (i.e. a larger  $\alpha$ ). We investigate this question in more details in Sec. 6.3.

#### 4.4 Hubble residuals

BayeSN Hubble residuals are defined as  $\Delta\mu = \mu_{\text{fit}} - \mu_{\text{cosmo}}$ , where  $\mu_{\text{cosmo}}$  are computed using the fiducial BayeSN cosmology (Flat  $\Lambda$ CDM with  $H_0 = 73.24$  and  $\Omega_m = 0.28$ , computed with [astropy Astropy Collaboration et al. 2013, 2018](#)). We subtract the mean of the Hubble residuals so that they are centred around zero. We compute SALT Hubble residuals using the [standax](#)<sup>4</sup> package. For the sake of comparison, we only use stretch and colour standardisation, and we do not include the environmental step correction, as this is not taken into account in the model used in this section. We discuss the inclusion of environmental dependencies in BayeSN in Sec. 5. We also do not include the broken- $\alpha$  found in [Ginolin et al. \(2025b\)](#). We use CMB-frame redshifts for both analyses. The comparison of Hubble residuals between SALT and BayeSN is plotted in Fig. 7. They are overall in good agreement. Some SNe Ia appear to have large Hubble residuals, but consistently in both methods, pointing towards either an outlier such as a peculiar subtype of SN Ia, or towards an issue with the light curve data itself.

We now focus on the Hubble residual scatter. The distribution of

<sup>4</sup> <https://github.com/mginolin/standax>

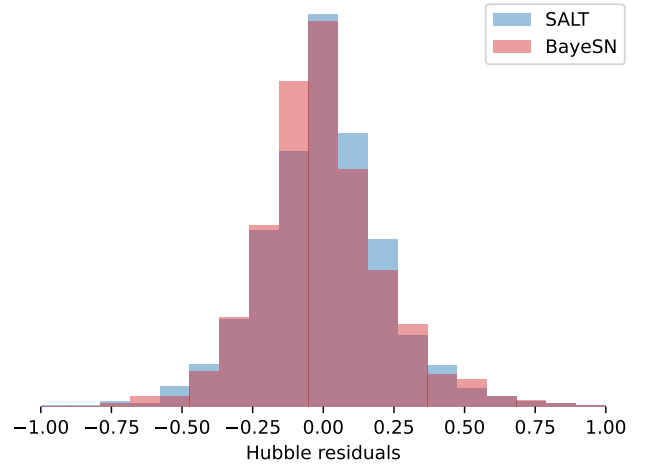


**Figure 8.** Histogram of (standardised) Hubble residuals, as computed in Sec. 4.4, for SALT and BayeSN.

**Table 2.** Magnitude steps (in mag) and their significances for the four DR2 environmental proxies. SALT steps are computed after standardisation, for a fair comparison, and are thus smaller than fiducial steps (as computed in [Ginolin et al. 2025b](#), see Sec. 4.5 for more details).

Step tracer	BayeSN	SALT
$(g - z)_{\text{local}}$	$0.086 \pm 0.010$ ( $8.3\sigma$ )	$0.089 \pm 0.010$ ( $8.5\sigma$ )
$(g - z)_{\text{global}}$	$0.080 \pm 0.010$ ( $7.8\sigma$ )	$0.083 \pm 0.010$ ( $7.9\sigma$ )
$\log(M_{\star}/M_{\odot})_{\text{local}}$	$0.070 \pm 0.010$ ( $6.8\sigma$ )	$0.087 \pm 0.011$ ( $8.2\sigma$ )
$\log(M_{\star}/M_{\odot})_{\text{global}}$	$0.103 \pm 0.010$ ( $10.1\sigma$ )	$0.099 \pm 0.010$ ( $9.5\sigma$ )

Hubble residuals, both for BayeSN and SALT, is plotted in Fig. 8. We present in Table 1 the value of the standard deviation  $\sigma_{\text{STD}}$  and the normalised Median Absolute Deviation  $\sigma_{\text{nMAD}}$ , as it is more robust to outliers. We compute those scatter both for the full sample, and for a subsample of SNe Ia for which the redshift comes from spectroscopic features of the host galaxy of the SN. We expect the scatter to be smaller for the host- $z$  sample, as the errors on  $z$  are of the order of  $\sigma_z \sim 10^{-4}$ , compared to the typical  $\sigma_z \sim 10^{-3}$  for redshifts coming from SNe features.

The scatter is slightly smaller for BayeSN residuals, compared to SALT residuals, both for the STD and nMAD, and for both the full sample and the host- $z$  sample. G26 come a similar conclusion, as they find a smaller scatter than SALT on their training sample, as well as an independent sample (DES5YY, [Popovic et al. 2026](#)). This confirms that the G26 BayeSN training performs well on a sample on which it was not trained.

#### 4.5 A posteriori steps

We here compute the leftover step in the BayeSN Hubble residuals, defined as the difference in Hubble residuals between two different SN environments, e.g. high- and low-mass hosts. This would be comparable to the a posteriori step (i.e. fitted after the SALT standardisation process) in [Ginolin et al. \(2025b\)](#). We use the same threshold value as in [Ginolin et al. \(2025a,b\)](#):

- Global mass:  $\log(M_{\star}/M_{\odot})_{\text{global}}^{\text{cut}} = 10$ .
- Local mass:  $\log(M_{\star}/M_{\odot})_{\text{local}}^{\text{cut}} = 8.9$ .

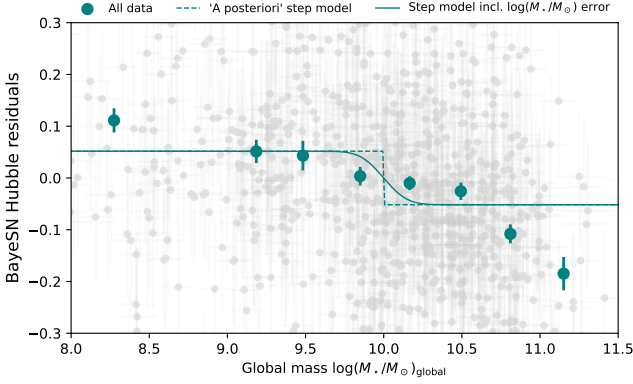


**Figure 9.** Hubble residuals for BayeSN light curve fits, as computed in Sec. 4.4, against host global stellar mass. The blue points are the mean residuals per bins of global mass. The bins are equally spaced, except for the edge ones that are slightly larger to encompass all points. The ‘a posteriori’ step model (see Sec. 4.5) is illustrated in the blue dashed line, while the full line shows the step model when convoluted with the mean error on  $\log(M_*/M_\odot)$ , as we account for these errors when computing the step.

- Local and global colour:  $(g - z)^{\text{cut}} = 1$ .

The proportion of SNe in each subsample defined by these cuts is roughly half-half (54% – 46% of SNe in locally red/blue environments, 57% – 43% for globally red/blue environments, 52% – 48% for locally high/low-mass environments, 53% – 47% for globally high/low-mass environments). We note that this method tends to underestimate the step compared to a full joint fit in the SALT framework, as some of the effect of the step is absorbed by the standardisation parameters ( $\alpha$  and marginally  $\beta$ ), and should thus not be used for standardisation purposes. It is however the only comparison currently available when using BayeSN in its fitting mode. The amplitude of the steps are compiled in Table 2, and we illustrate the global mass step in Fig. 9. We find consistent values within errorbars between SALT and BayeSN. The significance of the steps ranges between  $\sim 7 - 10\sigma$ , for both SALT and BayeSN. This confirms that the large steps found in Ginolin et al. (2025b) were not an artifact of SALT or of the SALT-based standardisation. We investigate more thoroughly the environmental steps in the next section.

## 5 INVESTIGATING THE ENVIRONMENTAL STEP

In this section, we leverage the explicit inclusion of dust impact on SN Ia light curves in BayeSN to investigate the relative contribution of intrinsic SED differences and dust to the observed environmental magnitude step.

### 5.1 Method

To investigate the step, we build on the analysis of Grayling et al. (2024), hereafter G24. This analysis splits the SN sample into two based on the value of the stellar mass of their host galaxy, to investigate differences in their absolute magnitude (i.e. the mass step) and the dust between the two subsamples, by introducing and fitting for population-level parameters to capture these effects. This method was tested on SALT-based simulations, which ensured it could correctly disentangle dust effects from an intrinsic step (Grayling & Popovic 2025). In this Section, contrary to Sec. 4, an individual  $R_V^s$  is inferred

for each SN. To obtain reasonable constraints on dust parameters, we thus condition distances on redshift and a cosmology (see Sec. 2.1). In G24, three different versions of the step training were presented. We here use the version in which the dust parameters ( $R_V^s$  and  $A_V^s$ , see Sec. 2) are drawn from two different populations, and an absolute magnitude offset is inferred between the two subsamples. We however extend the work of G24 on two points. First, we use the four environmental tracers available in the ZTF SN Ia DR2. The second change made is the introduction of a smooth step.

We illustrate this change using the global stellar mass  $M_*$  as the environmental tracer. In G24, the data is split sharply into two according to the host mass. The host galaxy  $R_V$  distribution is modelled as :

$$R_V^s \sim \begin{cases} \text{TN}(\mu_{R,\text{LM}}, \sigma_{R,\text{LM}}^2, 1.2, \infty) & \text{if } \log(M_*/M_\odot) \leq 10 \\ \text{TN}(\mu_{R,\text{HM}}, \sigma_{R,\text{HM}}^2, 1.2, \infty) & \text{if } \log(M_*/M_\odot) > 10 \end{cases}, \quad (2)$$

where TN denotes a truncated normal distribution, and the subscript LM/HM is used to distinguish parameters for the low- and high-mass sample. Similarly, the achromatic offset is drawn from:

$$\delta M^s \sim \begin{cases} N(\Delta M_0^{\text{LM}}, \sigma_{0,\text{LM}}^2) & \text{if } \log(M_*/M_\odot) \leq 10 \\ N(\Delta M_0^{\text{HM}}, \sigma_{0,\text{HM}}^2) & \text{if } \log(M_*/M_\odot) > 10 \end{cases}, \quad (3)$$

and the extinction is drawn from:

$$P(A_V^s | \tau_{A,\text{LM}}, \tau_{A,\text{HM}}) = \begin{cases} H(A_V^s) \times \tau_{A,\text{LM}}^{-1} \exp(-A_V^s/\tau_{A,\text{LM}}) & \text{if } \log(M_*/M_\odot) \leq 10 \\ H(A_V^s) \times \tau_{A,\text{HM}}^{-1} \exp(-A_V^s/\tau_{A,\text{HM}}) & \text{if } \log(M_*/M_\odot) > 10 \end{cases}. \quad (4)$$

However, this formulation does not take into account the measurement errors on the mass. Indeed, for an object near the split value, and with a noisy mass measurement, there is comparable chances that it is on either side of the mass split. We thus adapt the smooth step used in Ginolin et al. (2025b). For example, when using global mass as our environmental proxy, we compute for each SN a parameter  $p^s = \int_{-\infty}^{10} N(x | m^s, (\sigma_m^s)^2) dx$  where  $m^s = \log(M_*/M_\odot)$ . For each parameter, the value for a given SN is drawn for a mixture of the high- and low-mass distributions. In the case of  $R_V^s$ , this is modelled as as:

$$R_V^s \sim p^s \text{TN}(\mu_{R,\text{LM}}, \sigma_{R,\text{LM}}^2, 1.2, \infty) + (1 - p^s) \text{TN}(\mu_{R,\text{HM}}, \sigma_{R,\text{HM}}^2, 1.2, \infty). \quad (5)$$

A similar transformation is applied to the  $\delta M^s$  and  $A_V^s$  distributions.

We thus fit for ten hyperparameters:  $\Delta M_{0,\text{HM/LM}}$ ,  $\sigma_{0,\text{HM/LM}}$ ,  $\mu_{R,\text{HM/LM}}$ ,  $\sigma_{R,\text{HM/LM}}$  and  $\tau_{A,\text{HM/LM}}$ . We adopt the same hyperpriors as in G24. We proceed analogously when using the other three environmental tracers.

The impact of this smooth step is discussed in Sec. 6.2, and its implementation is available on GitHub<sup>5</sup>.

### 5.2 Dust parameters

We infer three dust parameters at the population level, for each of the two subsamples selected on environmental tracer: the mean and standard deviation of the  $R_V$  distribution  $\mu_{R,\text{HM/LM}}$  and  $\sigma_{R,\text{HM/LM}}$ , and the slope of the  $A_V$  distribution  $\tau_{A,\text{HM/LM}}$ .

<sup>5</sup> [github.com/mginolin/bayesn/tree/smooth\\_step](https://github.com/mginolin/bayesn/tree/smooth_step)

**Table 3.** Dust parameters split on environmental proxy (local and global colour, local and global mass). We also provide  $\mathbb{E}(R_V)$  and  $\sqrt{\text{Var}(R_V)}$  as they do not correspond to  $\mu_R$  and  $\sigma_R$ , since  $R_V$  is drawn from a truncated Gaussian distribution.

Sample	$\tau_A$	$\mu_R$	$\sigma_R$	$\mathbb{E}(R_V)$	$\sqrt{\text{Var}(R_V)}$
$(g-z)_{\text{local}} > 1$	$0.389 \pm 0.020$	$2.145 \pm 0.111$	$0.540 \pm 0.108$	$2.206 \pm 0.076$	$0.488 \pm 0.068$
$(g-z)_{\text{local}} < 1$	$0.341 \pm 0.020$	$2.325 \pm 0.121$	$0.577 \pm 0.109$	$2.371 \pm 0.101$	$0.535 \pm 0.077$
$(g-z)_{\text{global}} > 1$	$0.394 \pm 0.021$	$2.131 \pm 0.134$	$0.551 \pm 0.123$	$2.203 \pm 0.080$	$0.492 \pm 0.074$
$(g-z)_{\text{global}} < 1$	$0.348 \pm 0.021$	$2.296 \pm 0.139$	$0.603 \pm 0.123$	$2.358 \pm 0.103$	$0.550 \pm 0.082$
$\log(M_\star/M_\odot)_{\text{local}} > 8.9$	$0.475 \pm 0.024$	$2.220 \pm 0.092$	$0.527 \pm 0.088$	$2.261 \pm 0.075$	$0.488 \pm 0.062$
$\log(M_\star/M_\odot)_{\text{local}} < 8.9$	$0.272 \pm 0.018$	$2.274 \pm 0.175$	$0.610 \pm 0.136$	$2.347 \pm 0.124$	$0.550 \pm 0.086$
$\log(M_\star/M_\odot)_{\text{global}} > 10$	$0.395 \pm 0.021$	$2.164 \pm 0.110$	$0.500 \pm 0.100$	$2.207 \pm 0.083$	$0.461 \pm 0.069$
$\log(M_\star/M_\odot)_{\text{global}} < 10$	$0.359 \pm 0.021$	$2.249 \pm 0.149$	$0.681 \pm 0.129$	$2.352 \pm 0.100$	$0.597 \pm 0.078$

The values of each parameters are shown in Table 3, and a summary of the differences between dust properties is shown in Table 4 for all four environmental tracers. We do not detect any significant differences in  $R_V$ . The differences in mean  $R_V$  are similar to the ones from G24, and smaller than the ones found in Brout & Scolnic (2021) ( $\Delta\mathbb{E}(R_V) = 1.25 \pm 0.43$ ) and Popovic et al. (2023) ( $\Delta\mathbb{E}(R_V) = 0.89 \pm 0.45$ ), who both attribute all of the environmental step to dust variations.

The only significant change is the  $\sim 7\sigma$  difference in  $\tau_A$  when splitting on local mass. This is in line with results from Ginolin et al. (2025a), who found that local mass, along with  $d_{\text{DLR}}$ , had the biggest impact on dust attenuation, using the SALT colour distribution. Including a  $d_{\text{DLR}}$  dependency in the model would be an interesting avenue, especially in light of the results from Toy et al. (2025), who found a reduced mass step at high  $d_{\text{DLR}}$ , i.e. in the outskirts of galaxies.

### 5.3 Intrinsic steps

We show in Table 4 the estimates of the intrinsic steps, defined as  $\Delta M_0^{\text{LM}} - \Delta M_0^{\text{HM}}$ , for the four environmental tracers.

For every tracer, we detect a step at a  $> 3.5\sigma$  significance. This is a strong hint that the magnitude step in SNe Ia is not fully due to dust, and has a intrinsic component. This is in line with results from Ginolin et al. (2025a), who found that the steps did not significantly vary with colour, contrary to what is expected for a dust-based model of the step, where blue (e.g. unaffected by dust) SNe have a smaller step than red (e.g. dusty) SNe.

The ZTF steps are slightly larger than the one estimated by G24 from a compilation of Foundation, DES3Y and PS1MD SNe ( $0.049 \pm 0.016$  mag, a  $3.1\sigma$  significance). As the mean redshift of this sample is higher than the one of ZTF, this mismatch might be due to an evolution with redshift of the magnitude step. G24 also used a volume-limited sample in their analysis, which diminishes the probability of selection effects explaining the larger step found in ZTF.

There is a small trend of higher  $\tau_A$  and  $R_V$  differences leading to a smaller step. This is not surprising, as a larger variability in the extinction will lead to bigger differences in magnitudes, which then do not have to be compensated by the achromatic step.

The intrinsic steps found are smaller than the fiducial steps from Ginolin et al. (2025b) using a SALT-based standardisation, which ranged from  $\sim 0.12$  mag to  $\sim 0.17$  mag. This reduction might be due to the differing dust properties, which absorb part of the environmental dependencies of SN Ia absolute magnitude. Retraining

the model with an achromatic step and dust parameters common to all SNe gives slightly increased steps, with a local colour step of  $0.101 \pm 0.014$  ( $7.1\sigma$ ) and a global mass step of  $0.118 \pm 0.015$  ( $8.0\sigma$ ). However, a full retraining of the model including a step would be necessary to measure accurately the size of the step, so that all covariances between parameters are correctly accounted for. Indeed, as  $\theta_1$  is strongly correlated with environment (see Fig. 3),  $W_1$  might absorb some of the environment-magnitude correlation, leading to an overall smaller step.

## 6 DISCUSSION

In this section, we discuss variations of our analysis, as well as possible extensions for future work.

### 6.1 Impact of the training

To evaluate the impact of the use of the G26 training, we replicate our analysis with the training from T21. The biggest difference with our fiducial analysis is the scatter of the residuals, which are slightly larger than the SALT scatter for the full sample, and in line for the host- $z$  sample, as shown in Table 5. Moreover, the steps, either for the a posteriori case or the the ones from the retraining are all compatible, as shown in Table 6. There is a slight outlier ( $2.0\sigma$  difference between the T21 and G26 trainings for the a posteriori step in local mass), but this is not unexpected considering the number of parameters we infer. We thus conclude that all of the results from Secs. 4-5, bar the Hubble residual scatter, do not depend on the BayeSN training used.

### 6.2 Impact of the smooth step

To quantify the impact of using a smooth cut on environmental parameter, we run the analysis of Sec. 5 but using a sharp cut, as was done in G24. In the regular SALT standardisation framework, this inclusion of a smooth step pushes  $\gamma$  towards higher values, as it limits the impact of misspecified cases or SNe with large errors. In the case of BayeSN, this would impact both the achromatic step and the dust distribution, leading to a better separation of the two. The resulting steps and dust parameters are computed in Table 7. Implementing a smooth step pushed the step values higher, but within errorbars. This is in line with the behaviour seen in Ginolin et al. (2025b). The differences in dust properties,  $\Delta\mathbb{E}(R_V)$  and  $\Delta\tau_A$ , were also pushed higher by the inclusion of the smooth step.

**Table 4.** Environmental intrinsic step values ( $\Delta M_0^{\text{LM}} - \Delta M_0^{\text{HM}}$ ) for the G24 BayeSN model with modifications described in Sec. 5.1, along with differences in mean  $R_V$  and  $\tau_A$  between low-mass/blue and high-mass/red host galaxies.

Step tracer	Intrinsic step (mag)	$\Delta \mathbb{E}(R_V)$	$\Delta \tau_A$
$(g - z)_{\text{local}}$	$0.085 \pm 0.019 (4.5\sigma)$	$0.165 \pm 0.132 (1.2\sigma)$	$-0.047 \pm 0.028 (1.7\sigma)$
$(g - z)_{\text{global}}$	$0.072 \pm 0.019 (3.7\sigma)$	$0.155 \pm 0.126 (1.2\sigma)$	$-0.045 \pm 0.030 (1.5\sigma)$
$\log(M_\star/M_\odot)_{\text{local}}$	$0.081 \pm 0.019 (4.3\sigma)$	$0.086 \pm 0.148 (0.6\sigma)$	$-0.203 \pm 0.030 (6.8\sigma)$
$\log(M_\star/M_\odot)_{\text{global}}$	$0.103 \pm 0.018 (5.6\sigma)$	$0.146 \pm 0.139 (1.0\sigma)$	$-0.035 \pm 0.030 (1.2\sigma)$

**Table 5.** Same as Table 1 but for the T21 training.

Scatter	Full sample		Host-z sample	
	BayeSN	SALT	BayeSN	SALT
$\sigma_{\text{STD}}$	0.235	0.230	0.214	0.213
$\sigma_{\text{nMAD}}$	0.189	0.181	0.170	0.169

**Table 6.** Values of the magnitude steps (in mag) for the T21 training, either computed after light curve fits ('a posteriori', same as Table 2) or inferred as a population parameter accounting for different dust properties ('intrinsic', same as Table 4).

Step tracer	A posteriori steps	Intrinsic steps
$(g - z)_{\text{local}}$	$0.093 \pm 0.011 (8.6\sigma)$	$0.073 \pm 0.019 (3.9\sigma)$
$(g - z)_{\text{global}}$	$0.085 \pm 0.011 (7.9\sigma)$	$0.053 \pm 0.019 (2.8\sigma)$
$\log(M_\star/M_\odot)_{\text{local}}$	$0.099 \pm 0.011 (9.3\sigma)$	$0.064 \pm 0.019 (3.5\sigma)$
$\log(M_\star/M_\odot)_{\text{global}}$	$0.107 \pm 0.011 (10.0\sigma)$	$0.094 \pm 0.018 (5.3\sigma)$

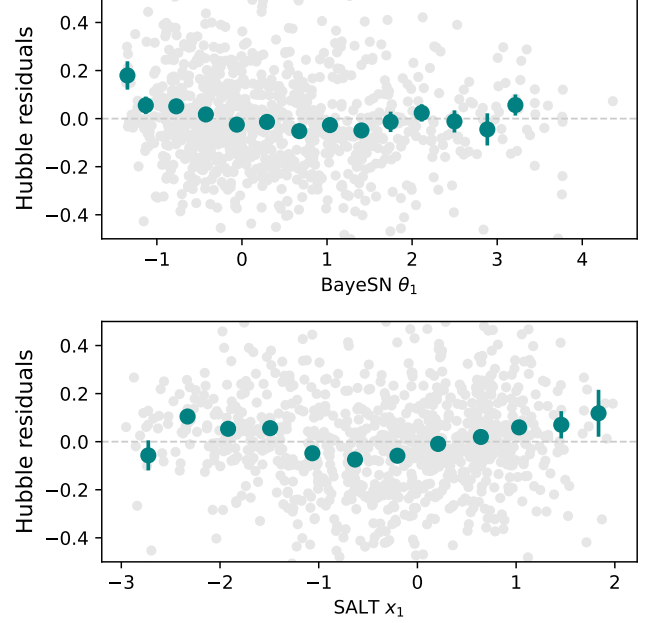
### 6.3 Non-linearity of the $\theta_1$ -Hubble residuals relation

In Ginolin et al. (2025b), a strong ( $\sim 13\sigma$ ) non linearity was found in the stretch-residuals relation (see also Garnavich et al. 2023; Larison et al. 2024; Rubin et al. 2026). This translated into two different standardisation coefficients  $\alpha$  for the two stretch regimes. In BayeSN, the surface  $W_1$  encapsulate both the changes in the shape of the SED and the slower-brighter relation, whereas in SALT-based standardisation, those two effects are separated into an  $M_1$  surface and an  $\alpha$  coefficient, such that  $\alpha \times M_1$  roughly corresponds to  $W_1$ . To investigate the existence of this non-linearity in BayeSN, we first look at any trend in the Hubble residuals- $\theta_1$  plane, as shown in the top of Fig. 10. As a point of reference, the same plot for SALT-standardised Hubble residuals is shown in the bottom panel of Fig. 10. There is not clear trend in the BayeSN Hubble residuals, contrary to the SALT ones. To quantify this effect, we refit the light curves but implementing a broken- $\alpha$  like standardisation in Eq. 1. We thus replace  $\theta_1^s \times W_1(t, \lambda)$  by:

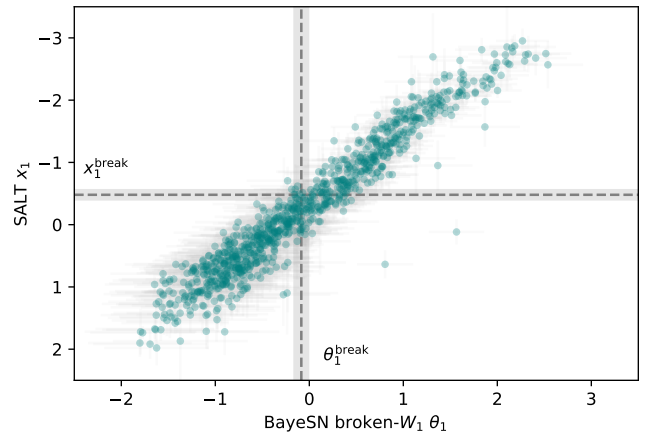
$$\begin{cases} \alpha_{\text{low}} \theta_1^s \times W_1(t, \lambda) & \text{if } \theta_1^s \leq \theta_1^{\text{break}} \\ (\alpha_{\text{high}} \theta_1^s + C) \times W_1(t, \lambda) & \text{if } \theta_1^s > \theta_1^{\text{break}} \end{cases} \quad (6)$$

This adds three hyperparameters to the model,  $\alpha_{\text{high}}$ ,  $\alpha_{\text{low}}$  and  $\theta_1^{\text{break}}$ .  $C$  is a constant that ensures continuity, and its value is fully determined by the set of  $(\alpha_{\text{high}}, \alpha_{\text{low}}, \theta_1^{\text{break}})$ . We then retrain the model, keeping  $W_0$ ,  $W_1$  and  $\Sigma_\epsilon$ , as well as the dust parameters  $R_V$  and  $\tau_A$ , fixed to their model value. As  $W_1$  is fixed, we have to add two coefficients, but if we were to retrain the full model, only one would be needed.

We find  $\alpha_{\text{low}} = 0.616 \pm 0.030$  and  $\alpha_{\text{high}} = 1.797 \pm 0.084$ . This is in accordance with the results from Ginolin et al. (2025b). Indeed, low  $\theta_1$ , i.e. high stretch, SNe are more standard than high  $\theta_1$  ones. More-



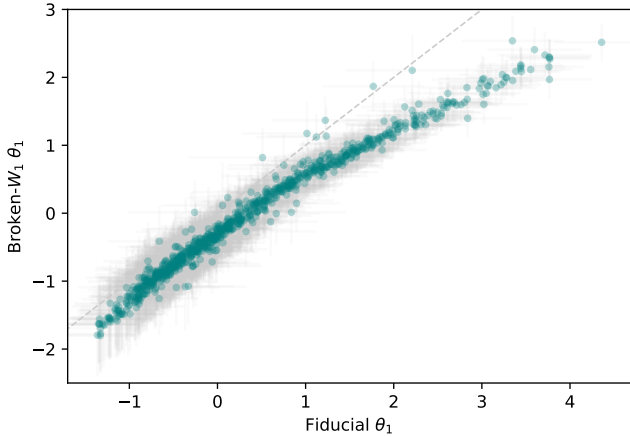
**Figure 10.** Hubble residuals, computed as described Sec. 4.4, against BayeSN  $\theta_1$  (top) and SALT  $x_1$  (bottom). The grey points are individual SNe and the blue points are binned averages, with the errorbars denoting the error on the mean.



**Figure 11.**  $\theta_1$  from the 'broken- $W_1$ ' model (see Sec. 6.3) against SALT  $x_1$ . The shaded bands represent the fitted  $\theta_1^{\text{break}}$  and  $x_1^{\text{break}}$  and the corresponding  $1\sigma$  errorbars.

**Table 7.** Same as Table 4 but for a sharp step, as done in G24.

Step tracer	Intrinsic step (mag)	$\Delta\mathbb{E}(R_V)$	$\Delta\tau_A$
$(g - z)_{\text{local}}$	$0.072 \pm 0.019$ ( $3.9\sigma$ )	$0.165 \pm 0.122$ ( $1.4\sigma$ )	$0.040 \pm 0.029$ ( $1.4\sigma$ )
$(g - z)_{\text{global}}$	$0.069 \pm 0.019$ ( $3.6\sigma$ )	$0.133 \pm 0.128$ ( $1.0\sigma$ )	$0.043 \pm 0.029$ ( $1.5\sigma$ )
$\log(M_\star/M_\odot)_{\text{local}}$	$0.075 \pm 0.020$ ( $3.8\sigma$ )	$0.070 \pm 0.135$ ( $0.5\sigma$ )	$0.190 \pm 0.030$ ( $6.4\sigma$ )
$\log(M_\star/M_\odot)_{\text{global}}$	$0.085 \pm 0.019$ ( $4.4\sigma$ )	$0.128 \pm 0.122$ ( $1.1\sigma$ )	$0.030 \pm 0.030$ ( $1.0\sigma$ )

**Figure 12.**  $\theta_1$  from the G26 BayeSN model (see Sec. 4.1.1) against  $\theta_1$  in the modified 'broken- $W_1$ ' model, as investigated in Sec. 6.3.

over, the difference in  $\alpha$  corresponds to  $\Delta\alpha = 1.181 \pm 0.090$ , as  $13.2\sigma$  difference, in line with the  $13.4\sigma$  level detected with SALT standardisation. We find  $\theta_1^{\text{break}} = -0.085 \pm 0.076$ , roughly corresponding to the SALT  $x_1^{\text{break}} \sim -0.5$ , as visible in Fig. 11.

However, in the BayeSN framework, refitting for those hyperparameters requires the joint fit of individual SN parameters, such as  $\theta_1^s$ . There is thus a degeneracy in the model, where the inclusion of  $\alpha_{\text{high/low}}$  can be counteracted with global shift of  $\theta_1$  values for high/low  $\theta_1$  SNe. This is visible in Fig. 12. While the low  $\theta_1$  SNe seem relatively unchanged from the fiducial fit of Sec. 4, the high  $\theta_1$  SNe see their  $\theta_1$  values being shifted lower by around  $\sim 1$ .  $A_V$  are largely unaffected. Looking at the comparison between SALT  $x_1$  and  $\theta_1$  when including the 'broken- $W_1$ ' relation in Fig. 11, they are now much more linearly correlated, without the curved tail visible at high  $\theta_1$  in Fig. 6. A tentative explanation of this behaviour is that the non-linear relation between BayeSN  $\theta_1$  and SALT  $x_1$  in the case of the fiducial model could be due to the model trying to grasp the  $\alpha$  non-linearity seen in SALT standardisation.

A principled way to account for these different standardisation relations for high- and low-stretch SNe would be to use a mixture model to account for two stretch populations, as was done in Rubin et al. (2026). This is however outside the scope of this work.

#### 6.4 Intrinsic SED variability between SNe from different environments

On top of fitting for an achromatic step, as we do in Sec. 5, G24 also investigated intrinsic SED differences between SNe in different environments by fitting for different  $W_0$  surfaces for SNe in high- and low-mass hosts. Their main finding was a strong difference in PS1  $i$ -band and PS1  $r$ - $i$  colour at  $\sim 20$  days after peak. We here

reproduce this analysis, adding the smooth transition between the two SN subpopulations as described in Sec. 5.1. For this analysis variation, we only split on global host mass. We use a slightly different post-processing than in G24, that we describe in Appendix A. This post-processing is needed to account for degeneracies between global shifts of  $\theta_1$  and changes in  $W_0$ .

Looking at Fig. 13, we see that the intrinsic SED differences between low- and high-mass SNe are stronger in  $i$ -band, especially at  $\sim 20$  days after peak. We measure a  $0.073 \pm 0.034$  mag ( $2.1\sigma$ ) step in peak  $g$ -band, a  $0.091 \pm 0.025$  mag ( $3.7\sigma$ ) step in peak  $r$ -band and a  $0.110 \pm 0.049$  mag ( $2.2\sigma$ ) step in peak  $i$ -band. While these step are smaller than the step in  $i$ -band at 20 days after peak ( $0.212 \pm 0.065$  mag,  $3.3\sigma$ ), the larger error in  $i$ -band, due to the poorer coverage (only half of the sample has  $i$ -band light curves, see Sec. 6.5), lowers its significance. These results confirm an intrinsic variability in SED between SNe in high- and low-mass hosts, which fluctuates with wavelength and time, as found in G24. When extending the SALT model to add an extra parameter  $x_2$ , Kenworthy et al. (2025) found that this parameter allowed for phase-dependent variations of colours curves, linked with the height of the  $i$ -band secondary maxima. Deckers et al. (2025) also found that standardising SNe with the strength of the light curve secondary maximum gave a better standardisation than using the SALT stretch  $x_1$ , which could be due to the fact that it encapsulates some of the magnitude step. Further constraining this variability, with large samples and wide wavelength coverage, might be an interesting avenue to understand the physical origin of the step.

#### 6.5 Full retraining

The current version of the ZTF SN Ia DR2 is not yet ready for cosmology. In particular, Lacroix et al. (2025) find a 90 mmag calibration uncertainty in magnitude, along with a 10 mmag shift in colour. Moreover, 52% of the SNe in the sample used in this analysis currently have detections in only two bands ( $g$  and  $r$ ), partly due to the lack of baseline measurements.

These issues are currently preventing the use of the DR2 as a training sample for BayeSN. Having sufficient wavelength coverage is particularly important to ensure sufficient constraints when inferring both intrinsic SED (e.g.  $W_0$  and  $W_1$ ) and dust properties ( $\mu_R$ ,  $\sigma_R$  and  $\tau_A$ ).

Nonetheless, these issues should be fixed with the upcoming release of ZTF scene-modelling light curves. This data will provide an interesting test case for training BayeSN, due to its large number of SNe, its homogeneity and its limited selection bias.

## 7 CONCLUSION

In this paper, we fit the ZTF SN Ia DR2 volume-limited sample with BayeSN. BayeSN is a hierarchical Bayesian model of SNe Ia at the SED level, which explicitly models the dust impact on SN Ia light curves. Our conclusions are the following:

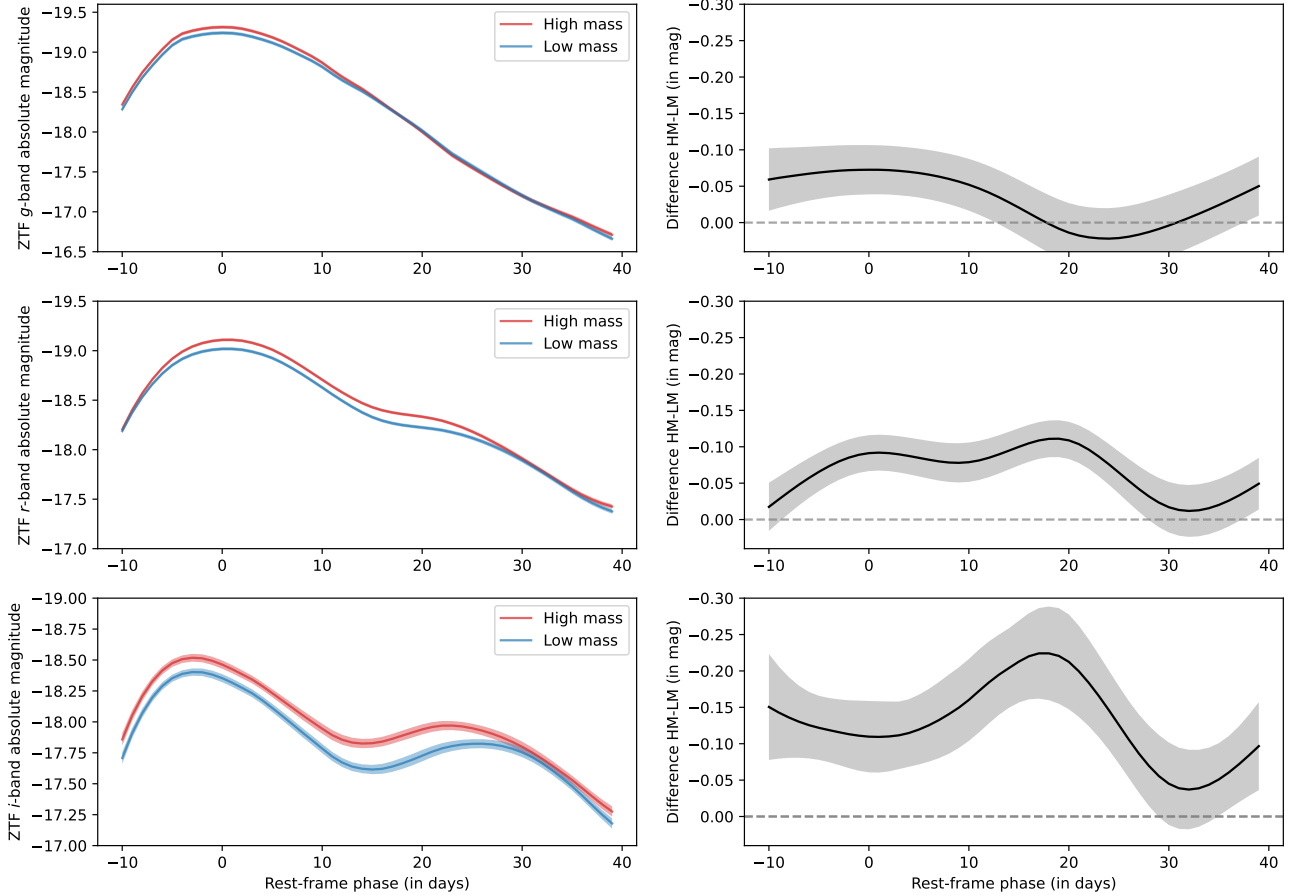


**Figure 13.** *Left:* Light curve of a  $A_V = 0$ ,  $\theta_1 = 0$ ,  $\epsilon = 0$  SN in a high-mass (red) and low-mass (blue) host galaxy, in ZTF  $g$ ,  $r$  and  $i$  bands. The model has been trained using the method in Sec. 6.4, and post-processed according to Appendix A. *Right:* Difference between the high- and low-mass models.

- Using the new G26 BayeSN training, we find a slightly reduced Hubble residuals scatter ( $\sigma_{\text{nMAD}} = 0.177$ ) than when using SALT ( $\sigma_{\text{nMAD}} = 0.181$ ). In comparison, the fiducial BayeSN model T21 gives  $\sigma_{\text{nMAD}} = 0.189$ .

- We find a scatter in SALT  $c$  for SNe with  $A_V = 0$ , hinting at an intrinsic SN colour scatter. Fitting SNe with low  $A_V$  ( $A_V < 0.1$ ), we find a characteristic  $c$  scatter of  $\sim 0.03$ , in line with the value from Ginolin et al. (2025a).

- We find a non-linearity between BayeSN  $\theta_1$  and SALT  $x_1$ . This might be due to an attempt of the BayeSN model to account for the strong non-linearity of the stretch-residuals relation (or broken- $\alpha$ ) found in Ginolin et al. (2025b).

- We find a  $0.103 \pm 0.010$  mag ( $10.1\sigma$ ) global mass step and a  $0.086 \pm 0.010$  ( $8.3\sigma$ ) local colour step when using the Hubble residuals from the BayeSN light curve fits, in accordance with the a posteriori SALT steps from Ginolin et al. (2025b). This means that the large steps seen in ZTF were not due to SALT or to the standardisation process.

- Accounting for different dust properties in high- and low-mass galaxies, we find a global mass step of  $0.103 \pm 0.018$  ( $5.6\sigma$ ) and a local colour step of  $0.085 \pm 0.019$  ( $4.5\sigma$ ). The difference in mean  $R_V$  between low- and high-mass galaxies is non-significant, respectively at  $\Delta\mathbb{E}(R_V) = 0.146 \pm 0.139$  ( $1.0\sigma$ ) for global mass and  $\Delta\mathbb{E}(R_V) = 0.165 \pm 0.132$  ( $1.2\sigma$ ) for local colour. We thus conclude that the environmental step is at least partially intrinsic.

Upcoming low-redshift SN Ia surveys, such as TITAN (Marlin et al. 2025), DEBASS (Sherman et al. 2025) and YSE (Jones et al. 2021), will be valuable to understand the origin of the large step in the ZTF sample. Detailed studies of the host environment of SNe Ia, using either multi-bands host galaxy measurements (e.g. Ramaiya et al. 2025) or simulations (e.g. Wiseman et al. 2022), will also bring insight into the origin of the step. Nevertheless, our results reaffirm the strength of this effect, and thus the need to correctly account for it in cosmological analyses to guarantee unbiased cosmological parameter inference.

## ACKNOWLEDGEMENTS

Supernova and astrostatistics research at Cambridge University is supported in part by the European Union’s Horizon 2020 research and innovation programme under European Research Council Grant Agreement No 101002652 (BayeSN; PI K. Mandel). LK acknowledges support for an Early Career Fellowship from the Leverhulme Trust through grant ECF-2024-054 and the Isaac Newton Trust through grant 24.08(w).

## DATA AVAILABILITY

The data used in this analysis can be downloaded from [ztfcosmo.in2p3.fr](http://ztfcosmo.in2p3.fr). The BayeSN code is available at

[github.com/bayesn](https://github.com/bayesn), its version used for this article is available at [github.com/mginolin/bayesn](https://github.com/mginolin/bayesn), and the `standax` code is available at [github.com/mginolin/standax](https://github.com/mginolin/standax).

## REFERENCES

- Abbott T. M. C., et al., 2019, *ApJ*, 872, L30
- Adame A. G., et al., 2025, *J. Cosmology Astropart. Phys.*, 2025, 021
- Amanullah R., et al., 2010, *ApJ*, 716, 712
- Amenouche M., et al., 2025, *A&A*, 694, A3
- Astier P., et al., 2006, *A&A*, 447, 31
- Astropy Collaboration et al., 2013, *A&A*, 558, A33
- Astropy Collaboration et al., 2018, *AJ*, 156, 123
- Bellm E. C., et al., 2019, *PASP*, 131, 018002
- Betoule M., et al., 2014, *A&A*, 568, A22
- Blagorodnova N., et al., 2018, *PASP*, 130, 035003
- Briday M., et al., 2022, *A&A*, 657, A22
- Brout D., Scolnic D., 2021, *ApJ*, 909, 26
- Brout D., et al., 2022, *ApJ*, 938, 110
- Carr A., Davis T. M., Scolnic D., Said K., Brout D., Peterson E. R., Kessler R., 2022, *Publ. Astron. Soc. Australia*, 39, e046
- Carrick J., Turnbull S. J., Lavaux G., Hudson M. J., 2015, *MNRAS*, 450, 317
- Chambers K. C., et al., 2016, arXiv e-prints, p. arXiv:1612.05560
- Childress M., et al., 2013, *ApJ*, 770, 108
- Childress M. J., Wolf C., Zahid H. J., 2014, *MNRAS*, 445, 1898
- DES Collaboration et al., 2024, *ApJ*, 973, L14
- DESI Collaboration et al., 2025, arXiv e-prints, p. arXiv:2503.14738
- Deckers M., et al., 2025, *A&A*, 694, A12
- Dekany R., et al., 2020, *PASP*, 132, 038001
- Di Valentino E., et al., 2025, arXiv e-prints, p. arXiv:2504.01669
- Duarte J., et al., 2023, *A&A*, 680, A56
- Filippenko A. V., 1989, *PASP*, 101, 588
- Fitzpatrick E. L., 1999, *PASP*, 111, 63
- Foley R. J., et al., 2018, *MNRAS*, 475, 193
- Freedman W. L., 2021, *ApJ*, 919, 16
- Garnavich P., et al., 2023, *ApJ*, 953, 35
- Ginolin M., et al., 2025a, *A&A*, 694, A4
- Ginolin M., et al., 2025b, *A&A*, 695, A140
- González-Gaitán S., de Jaeger T., Galbany L., Mourão A., Paulino-Afonso A., Filippenko A. V., 2021, *MNRAS*, 508, 4656
- Graham M. J., et al., 2019, *PASP*, 131, 078001
- Grayling M., Popovic B., 2025, *MNRAS*, 542, 2060
- Grayling M., Thorp S., Mandel K. S., Dhawan S., Uzsoy A. S. M., Boyd B. M., Hayes E. E., Ward S. M., 2024, *MNRAS*, 531, 953
- Grayling M., et al., 2026, *MNRAS*, 548, stag340
- Gupta R. R., et al., 2016, *AJ*, 152, 154
- Guy J., Astier P., Nobili S., Regnault N., Pain R., 2005, *A&A*, 443, 781
- Guy J., et al., 2007, *A&A*, 466, 11
- Guy J., et al., 2010, *A&A*, 523, A7
- Hamuy M., Phillips M. M., Suntzeff N. B., Schommer R. A., Maza J., Smith R. C., Lira P., Aviles R., 1996, *AJ*, 112, 2438
- Hayes E. E., et al., 2025, *MNRAS*, 541, 1948
- Hicken M., et al., 2009a, *ApJ*, 700, 331
- Hicken M., Wood-Vasey W. M., Blondin S., Challis P., Jha S., Kelly P. L., Rest A., Kirshner R. P., 2009b, *ApJ*, 700, 1097
- Hicken M., et al., 2012, *ApJS*, 200, 12
- Holtzman J. A., et al., 2008, *AJ*, 136, 2306
- Hsiao E. Y., Conley A., Howell D. A., Sullivan M., Pritchett C. J., Carlberg R. G., Nugent P. E., Phillips M. M., 2007, *ApJ*, 663, 1187
- Jha S., Riess A. G., Kirshner R. P., 2007, *ApJ*, 659, 122
- Jones D. O., et al., 2018, *ApJ*, 857, 51
- Jones D. O., et al., 2021, *ApJ*, 908, 143
- Kelly P. L., Hicken M., Burke D. L., Mandel K. S., Kirshner R. P., 2010, *ApJ*, 715, 743
- Kelsey L., et al., 2021, *MNRAS*, 501, 4861
- Kelsey L., et al., 2023, *MNRAS*, 519, 3046
- Kenworthy W. D., et al., 2021, *ApJ*, 923, 265
- Kenworthy W. D., et al., 2025, arXiv e-prints, p. arXiv:2502.09713
- Kim Y.-L., Smith M., Sullivan M., Lee Y.-W., 2018, *ApJ*, 854, 24
- Krisciunas K., et al., 2017, *AJ*, 154, 211
- Lacroix L., et al., 2025, arXiv e-prints, p. arXiv:2509.04073
- Lampeitl H., et al., 2010, *ApJ*, 722, 566
- Larison C., Jha S. W., Kwok L. A., Camacho-Neves Y., 2024, *ApJ*, 961, 185
- Magee M. R., 2026, arXiv e-prints, p. arXiv:2604.22928
- Mandel K. S., Wood-Vasey W. M., Friedman A. S., Kirshner R. P., 2009, *ApJ*, 704, 629
- Mandel K. S., Narayan G., Kirshner R. P., 2011, *ApJ*, 731, 120
- Mandel K. S., Scolnic D. M., Shariff H., Foley R. J., Kirshner R. P., 2017, *ApJ*, 842, 93
- Mandel K. S., Thorp S., Narayan G., Friedman A. S., Avelino A., 2022, *MNRAS*, 510, 3939
- Mannucci F., Della Valle M., Panagia N., 2006, *MNRAS*, 370, 773
- Marlin E. G., et al., 2025, arXiv e-prints, p. arXiv:2512.21903
- Masci F. J., et al., 2019, *PASP*, 131, 018003
- Müller-Bravo T., Galbany L., 2022, *The Journal of Open Source Software*, 7, 4508
- Nicolas N., et al., 2021, *A&A*, 649, A74
- Perley D. A., et al., 2020, *ApJ*, 904, 35
- Perlmutter S., et al., 1999, *ApJ*, 517, 565
- Phillips M. M., 1993, *ApJ*, 413, L105
- Popovic B., Brout D., Kessler R., Scolnic D., 2023, *ApJ*, 945, 84
- Popovic B., et al., 2024, *MNRAS*, 534, 2263
- Popovic B., et al., 2025a, arXiv e-prints, p. arXiv:2506.05471
- Popovic B., et al., 2025b, *A&A*, 694, A5
- Popovic B., et al., 2026, *MNRAS*,
- Ramaiya S., Vincenzi M., Jarvis M. J., Wiseman P., Sullivan M., 2025, *MNRAS*, 543, 2180
- Riess A. G., et al., 1998, *AJ*, 116, 1009
- Riess A. G., et al., 2022, *ApJ*, 934, L7
- Rigault M., et al., 2013, *A&A*, 560, A66
- Rigault M., et al., 2015, *ApJ*, 802, 20
- Rigault M., et al., 2019, *A&A*, 627, A115
- Rigault M., et al., 2020, *A&A*, 644, A176
- Rigault M., et al., 2025, *A&A*, 694, A1
- Rubin D., et al., 2023, arXiv e-prints, p. arXiv:2311.12098
- Rubin D., Hoyt T., Aldering G., Perlmutter S., 2026, arXiv e-prints, p. arXiv:2601.19854
- Sarin N., et al., 2026, arXiv e-prints, p. arXiv:2602.02677
- Sherman N. F., et al., 2025, arXiv e-prints, p. arXiv:2508.10878
- Smith M., et al., 2012, *ApJ*, 755, 61
- Sullivan M., et al., 2006, *ApJ*, 648, 868
- Sullivan M., et al., 2010, *MNRAS*, 406, 782
- Taylor G., Lidman C., Tucker B. E., Brout D., Hinton S. R., Kessler R., 2021, *MNRAS*, 504, 4111
- Thorp S., Mandel K. S., 2022, *MNRAS*, 517, 2360
- Thorp S., Mandel K. S., Jones D. O., Ward S. M., Narayan G., 2021, *MNRAS*, 508, 4310
- Toy M., et al., 2025, *MNRAS*, 538, 181
- Tripp R., 1998, *A&A*, 331, 815
- Uddin S. A., et al., 2020, *ApJ*, 901, 143
- Uzsoy A. S. M., Thorp S., Grayling M., Mandel K. S., 2024, *MNRAS*, 535, 2306
- Vincenzi M., et al., 2024, *ApJ*, 975, 86
- Wiseman P., et al., 2022, *MNRAS*, 515, 4587

## APPENDIX A: POST-PROCESSING OF THE MODEL FOR THE INTRINSIC SED VARIABILITY

Looking at Eq. 1, there exists a degeneracy between the definition of  $\theta_1$  and  $W_0$ . Indeed, a global shift of  $\theta_1 \rightarrow \theta_1 + A$  combined with a shift of  $W_0 \rightarrow W_0 - A \times W_1$  leaves the model unchanged. This degeneracy is partially broken by the use of a prior on  $\theta_1$ , but it means that the definition of  $\theta_1$  is tied to the data the model was trained on. This comes as an issue when training separately on a high and low-mass subsample, as done in Sec. 6.4, where both subsamples will end up with a  $\theta_1$  distribution mean around 0, whereas their light curve widths are on average different (see Fig. 3). As this  $\theta_1$  shift then affects  $W_0$ , some post-processing of the output parameters is needed in order to be able to compare the high and low-mass SEDs. The post-processing used in G24 anchored  $\theta_1$  to the decline rate in PS1-g-band  $\Delta m_{15}$ , so that SNe in a high and low-mass galaxy with  $\theta_1 = 0$ ,  $A_V = 0$ ,  $\epsilon = 0$  had the same  $\Delta m_{15}$ . However, this post-processing relied on two hypotheses (independence of  $\frac{\partial \Delta m_{15}}{\partial \theta_1}$  on  $\Delta m_{15}$ , independence of  $\Delta m_{15}$  on  $A_V$ ), valid when using the T21 model but no longer verified with the G26 model. This may be due to the wider range of colour and light curve widths spanned by the G26 training sample, probing parameter spaces unexplored before, as well as the non-linearity of the light-curve width-magnitude relation, that the currently linear BayeSN model does not account for. We thus modify the post-processing so that the  $\theta_1$  distributions are anchored to the ones previously obtained when fitting for an achromatic intrinsic step, as in Sec. 5. We compute the low- and high-mass  $\theta_1$  shifts as:

$$\Delta\theta_1^{\text{LM}} = \frac{\sum_s p^s (\theta_{1, \text{SED}}^s - \theta_{1, \text{ref}}^s)}{\sum_s p^s}, \quad (\text{A1})$$

$$\Delta\theta_1^{\text{HM}} = \frac{\sum_s (1 - p^s) (\theta_{1, \text{SED}}^s - \theta_{1, \text{ref}}^s)}{\sum_s (1 - p^s)}, \quad (\text{A2})$$

where  $\theta_{1, \text{ref}}$  is the reference  $\theta_1$  value when fitting for an achromatic step, and  $p^s$  is the probability of a given SN to have a low-mass host (see Sec. 5.1). We then correct the  $W_0$  surfaces using  $W_0^{\text{LM/HM}} \rightarrow W_0^{\text{LM/HM}} - \Delta\theta_1^{\text{HM}} W_1$ .

This paper has been typeset from a  $\text{\LaTeX}$  file prepared by the author.